Computation of Aeroacoustic Phenomena in Subsonic and Transonic Ducted Flows

Thomas Emmert* and Philippe Lafon†

Laboratoire de Mécanique des Structures Industrielles Durables,

UMR CNRS EDF 2823, Clamart, France

Christophe Bailly‡

Laboratoire de Mécanique des Fluides et d'Acoustique,

École Centrale de Lyon & UMR CNRS 5509, Ecully, France

A sonic flow in a plane duct passing an abrupt increase in cross-section is numerically studied by solving the 3-D compressible Navier-Stokes equations. Different flow patterns are likely to appear in such configuration. For a very low downstream pressure, the flow is entirely supersonic. For higher pressures, unstable flow patterns emerge. One of these patterns features a normal shock, that oscillates due to a self-exciting mechanism. As the duct is open at the outflow, aeroacoustic coupling occurs when the shock oscillations get in resonance with the longitudinal acoustic modes of the duct. The main flow features are well captured by the present numerical simulations but no coupling with longitudinal duct modes is found. The governing equations are solved using high-order methods based on central finite differences. To damp out spurious oscillations supported by central differences selective filtering and a well established non-linear shock-capturing term are used. A high-order overset grid approach is implemented in order to tackle with complex geometries.

Contents

*PhD student

†Research engineer, AIAA member

‡Professor, AIAA member

I. Introduction

Strong interactions between shock oscillations, internal aerodynamic noise and acoustic duct modes are often observed in confined flows but are undesirable to prevent excitation of structural vibrations and fatigue. Numerous examples can be found in the review of Meier *et al.*[1]

In the present work, a transonic flow passing a sudden expansion in a duct is studied. This kind of flow can be found downstream of control devices such as valves encountered in pipe systems of power plants, and has been investigated experimentally by Meier *et al.*[2] These authors studied a transonic flow in a rectangular duct such as displayed in Figure 1. Air at atmospheric conditions (denoted by subscript a) passes through a convergent nozzle. The flow in the nozzle throat is expanded abruptly by passing in the expansion duct of larger cross-section. The flow is driven by the exit pressure p_e in the reservoir downstream of the expansion duct. Different transonic and supersonic flow regimes have been investigated as a function of the pressure ratio defined by $\tau = p_e/p_a$.

For very low pressure ratios the flow in the upstream part of the test duct is entirely supersonic. The flow regime for $\tau = 0.15$ is visualized by means of Mach-Zehnder Interferometry[2] in Figure 2 (a). A system of crossing oblique shock waves is observed. Increasing the exit pressure leads to a flow separation and to a breakdown of the shock cell structure. Shock pattern oscillations are then observed. If the downstream pressure is further increased, the oblique shock wave system disappears and the supersonic expansion ends up after a single normal shock such as presented in Figure 2 (b) for $\tau = 0.348$. In this case, a strong coupling between the self sustained oscillations of the normal shock and the longitudinal acoustic modes of the duct is found. The observed oscillation frequencies are low ($O(10^2)$ Hz). For lower pressure ratios the flow regime is symmetrical. For higher pressure ratios asymmetric flow pattern occurs and one side is entirely separated from the wall such as shown in Figure 2 (c). For those flows, having a more jet like structure, a coupling mechanism similar to the normal shock configuration, is only observed for longer ducts. Meier *et al.*[2] provide time sequence visualizations of the different flow regimes based on Mach-Zehnder Interferometry. Static wall pressure data, frequency spectra and cross correlations of the pressure fluctuations along the walls are also available, making possible a quantitative validation of the numerical results.

This flow configuration involving turbulence, shocks, interaction with boundary layers and aeroacoustic resonances is a real challenge for computational aeroacoustics.[3] The numerical algorithm must be robust in order to treat shocks and wall flows and also preserve acoustic waves and sound pressure level peaks that result from complex non-linear interactions. Devos and Lafon[4] studied numerically this configuration using a second-order TVD finite-volume scheme for solving 2-D Euler equations. The main flow patterns were captured but the coupling of the shock oscillations with the resonance modes of the duct was not considered. In this work a numerical solver of the Navier-Stokes equations, called SAFARI (Simulation of Aeroacoustic Flows And Resonance and Interaction), has been developed to simulate aeroacoustic couplings for internal flows in complex geometries. High-order schemes are used to preserve the generated acoustic field and a non-linear adaptive filter is implemented to capture strong shock waves. A high-order overset grid ability has been adapted in the code in order to treat complex geometries.

The paper is organized as follows. The numerical algorithm is briefly discussed in section II. In section III the supersonic flow at a low pressure ratio $\tau = 0.15$ is presented. In section IV four simulations are presented for pressure ratios involving a normal shock flow pattern in order to demonstrate the numerical evidence of coupling of shock oscillations with the duct modes. Then, concluding remarks are given in section V. In Appendix A, the numerical algorithm is applied to subsonic ducted cavity flows.

II. Governing equations and numerical algorithm

The set of equations are the compressible 3-D Navier-Stokes equations, written in conservative form after application of a general time-invariant curvilinear coordinate transformation from physical space to computational space $(x, y, z) \to (\xi, \eta, \zeta)$. This yields

$$\frac{\partial}{\partial t}\Big(\frac{\mathbf{Q}}{J}\Big) + \frac{\partial \mathbf{E}}{\partial \xi} + \frac{\partial \mathbf{F}}{\partial \eta} + \frac{\partial \mathbf{G}}{\partial \zeta} = 0,$$

where J is the Jacobian of the geometric transformation. The unknown vector in the above equation writes $\mathbf{Q} = (\rho, \rho u, \rho v, \rho w, \rho e_t)^T$, where ρ designates the density, u, v, w the Cartesian velocity components and ρe_t the total energy. The latter is calculated for a perfect gaz for which $\rho e_t = p/(\gamma - 1) + \rho(u^2 + v^2 + w^2)$. The

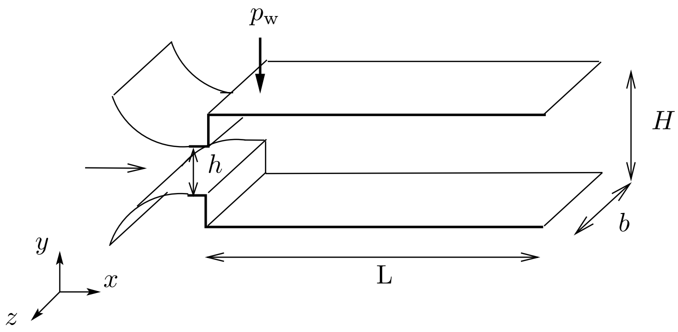

Figure 1. Transonic flow passing sudden expansion: sketch of the geometry and notations: H and L are the height and the length of the expansion duct respectively, h designates the height of the inflow nozzle and $b = 0.1$m is the width of the nozzle and the expansion duct in spanwise direction. p_a and T_a are the pressure and temperature of air at ambient conditions. p_e is the pressure in the downstream reservoir imposed by the pressure ratio $\tau = p_e/p_a$. p_w is the pressure in the corner region.

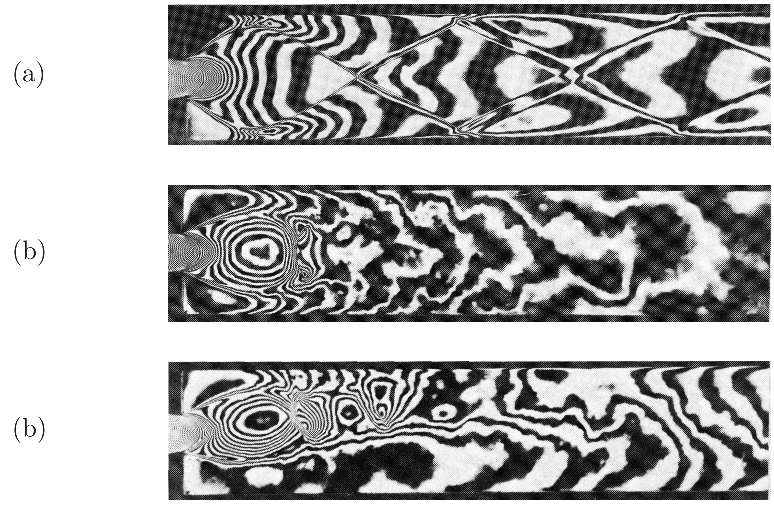

Figure 2. Mach-Zehnder interferometry visualizations at pressure ratios: (a) $\tau = 0.15$ (b) $\tau = 0.348$ for a expansion duct length $\mathbf{L} = 0.24$ m and aspect ratios $\mathbf{L/H} = 7.23$ and $\mathbf{h/H} = 0.3$.[2]

flux vectors **E**, **F**, **G** contain the inviscid and the viscous terms. Their expressions as well as the metric identities for the grid transformation can be found in the work of Visbal and Gaitonde or Marsden *et al.*[5,6] The viscosity is determined by Sutherland's law:

$$\frac{\mu}{\mu_{\text{ref}}} = \left(\frac{T}{T_{\text{ref}}}\right)^{3/2} \frac{T_{\text{ref}} + C}{T + C}$$

where $T_{\text{ref}} = 273$ K is the ambient temperature. The fluid dependent parameters for air are taken to be $\mu_{\text{ref}} = \mu(T_{\text{ref}}) = 1.5 \times 10^{-5}$ kg.m^{-1}.s^{-1} and $C = 110$ K.[7]

For interior points of the computational domain, the fluxes and the velocity derivatives for the viscous terms are discretized by the centered 11-point finite difference scheme developed by Bogey and Bailly.[8] This scheme has been optimized in wave number space and is able to resolve accurately perturbations with only four points per wavelength. An explicit fourth-order low-storage Runge-Kutta scheme advances the solution in time. The CFL number is 0.9 and the time step Δt is updated every iteration during the transient phase. An appropriate optimized explicit 11-point low pass filter remove grid-to-grid oscillations, not resolved by centered finite difference schemes.[8] At the same time the filter removes properly the non-resolved turbulent structures and acts like a subgrid scale model. This method has been successfully applied by Bogey *et al.*[9] and by Visbal *et al.*[10] The filtering coefficient is chosen to be 0.2 inside the computational domain.

In regions with strong shocks, additional numerical dissipation is introduced by using the adaptive non-linear artificial dissipation model of Kim and Lee.[11] In the present computations the second-order filter is applied in the computational space. It yields:

$$\mathbf{Q}^{n+1}_{i,j,k} = \hat{\mathbf{Q}}^{n+1}_{i,j,k} - (\mathbf{D}_{i+\frac{1}{2},j,k} - \mathbf{D}_{i-\frac{1}{2},j,k}),$$

where

$$\mathbf{D}_{i+\frac{1}{2},j,k} = \frac{\Delta|\lambda|^{\text{stencil}}_{i+\frac{1}{2},j,k}}{\frac{1}{2}(J_{i+1,j,k} + J_{i,j,k})}\ \epsilon^{(2)}_{i+\frac{1}{2},j,k}\ \Delta t\big(\hat{\mathbf{Q}}_{i+1,j,k} - \hat{\mathbf{Q}}_{i,j,k}\big).$$

$\hat{\mathbf{Q}}$ is the unknown vector that has already been treated by the linear selective filter. The quantity $\Delta|\lambda|^{\text{stencil}}_{i+1/2,j,k}$ denotes the difference between the greatest and the smallest eigenvalue

$$|\lambda|_{i,j,k} = \left(|U| + c\sqrt{\xi_x^2 + \xi_y^2 + \xi_z^2}\ \right)_{i,j,k}$$

within a stencil of variable size. The quantities U and c designates the contravariant velocity $U = u\xi_x + v\xi_y + w\xi_z$ and the speed of sound respectively. According to Kim and Lee a stencil width of 7 points is chosen:

$$\Delta|\lambda|^{\text{stencil}}_{i+\frac{1}{2},j,k} = \max_{m=-2}^{3}\ (|\lambda|_{i+m,j,k}) - \min_{m=-2}^{3}\ (|\lambda|_{i+m,j,k})\,.$$

In order to ensure a high-quality solution, the second-order filter may only be applied locally in the shock region. This is performed by the adaptive non-linear function $\epsilon^{(2)}_{i+1/2,j,k}$ that reaches its maximum in regions of strong shocks and is very small in smooth regions. The shock position is detected by using the curvature of the pressure such as proposed by Jameson.[12] Further details about the detection procedure are available in the work of Kim and Lee.[11] The filtering, selective and shock-capturing filter, is applied after each Runge-Kutta cycle.

The implemented finite difference schemes are limited to structured grids. In order to treat more complex geometries, a high-order overset ability has been adapted and implemented in the code. In this approach the computational domain is subdivided into overlapping structured grid components. The governing equations are solved on each component grid separately and domain connectivity is obtained through the use of interpolation. Also known as the Chimera grid method, this approach has been proposed first by Benek *et al.*[13] and extended for aeroacoustic simulations by Delfs.[14] For grid generation *ogen*, the grid assembler module of the freely available library *Overture* developed at the Lawrence Livermore National Laboratory, has been interfaced with the code.[15] The conception of *Overture* as a library makes it easy to call grid assembler functions during the simulation and makes the simulation multiple bodies in relative motion and fluid structure interactions problems possible. For communication between grid boundaries that do not coincide, high-order interpolation is used. Lagrangian polynomials has been found by Sherer and Scott[16] to be best suited in terms of precision, execution time and implementation aspects for the high-order overset grid approach. Various tests have shown that at least eight-order polynomials have to be used in order to make the error of the interpolation negligible when using the 11-points difference scheme.

For load balancing purpose, each component grid can be subdivided evenly N times in each direction and can be computed by $N_{\text{procs}} = N_{\xi,\text{procs}} \times N_{\eta,\text{procs}} \times N_{\zeta,\text{procs}}$. In a preprocessing step, SAFARI distributes the data concerning the computational grid and the interpolation provided by *ogen* for the parallel computation. The standard Message Passing Interface (MPI) library routines have been used for code parallelization.

III. Supersonic flow at low pressure ratio ($\tau = 0.15$)

1. *Simulation parameters*

The entire overset grid generated by *ogen* is represented in Figure 3 (a). It consists of three parts: the nozzle, the expansion duct and the reservoir. Note that the convergent part of the nozzle is not modeled in this work. The inflow conditions are determined assuming the flow to be isentropic in the convergent part. The grid points in the nozzle and in the expansion duct are spaced uniformly in each direction. The reservoir grid is stretched in x-direction on the last 30 points and in y-direction on the last 50 points with a ratio of 3% and 1% respectively. The grid in the spanwise z-direction is also spaced uniformly.

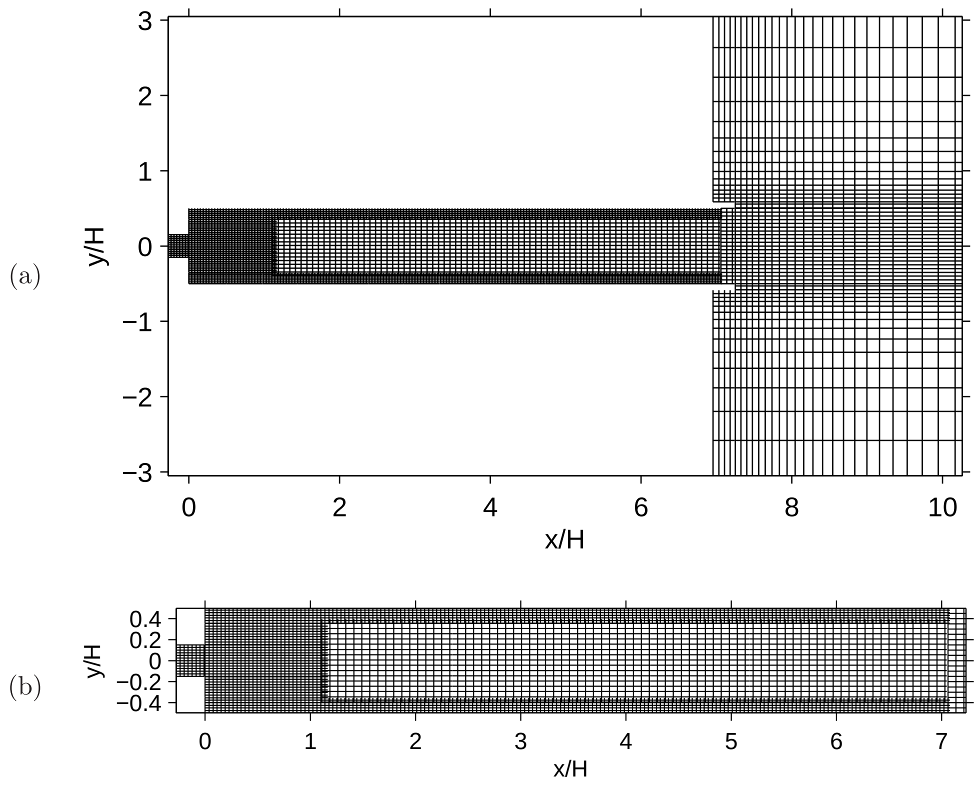

Figure 3. Visualization of the overset grid in the $x - y$ plane such as generated by *ogen* for the pressure ratio $\tau = 0.15$. The geometric parameters are $L = 0.24$ m, L/H $= 7.23$ and h/H $= 0.3$. Every eighth line is represented. Figure (a) shows the complete computational domain: the nozzle, the expansion duct and the outflow reservoir. Figure (b) is a detailed view on the nozzle and the expansion duct. The walls are refined using overlapping grids.

For the low pressure ratio case shocks interact with the boundary layers developing along the walls of the expansion duct, a fine grid resolution in these regions is required. This can be accomplished easily by the overset grid approach that allows to patch grids of arbitrarily refinement in the regions of interest as shown in Figure 3 (b). Refined grids has been used to mesh the nozzle and the near wall zone of the expansion duct. More details about the grid sizes in wall units are given in Table 1.

	N_x	N_y	N_z	Δx^+_{min}	Δy^+_{min}	Δz^+_{min}	N_{procs}
Nozzle	58	98	41	12	8	24	2
Expansion duct	744	127	41	24	16	24	22
Near wall grid	1439	47	41	12	8	24	2×9
Reservoir	180	398	41	24	16	24	16

Table 1. Mesh characteristics for the low pressure ratio case $\tau = 0.15$. The total number of 14×10^6 grid points have been distributed over $N_{\mathbf{procs}} = 58$ processors. The length scales are given in wall units: $y^+ = y u_f \rho/\mu$. The friction velocity u_f is determined near the outflow at $x = 0.2$ m.

The pressure and temperature of air at rest in the upstream reservoir (not considered in the simulation) is provided by the experiments $p_a = 101325$ Pa and $T_a = 293$ K. The sonic conditions imposed at the nozzle inflow are computed using isentropic relations :

$$M_{in} = u_{in}/c_{in} = 1.01,\ v_{in} = 0,\ p_{in} = 0.5221\ p_a,\ T_{in} = 0.8306\ T_a.$$

The velocity profile in the nozzle is kept uniform by applying slip wall conditions. This approximation is justified as the nozzle length is short and the developing boundary layer is expected to be very thin. The

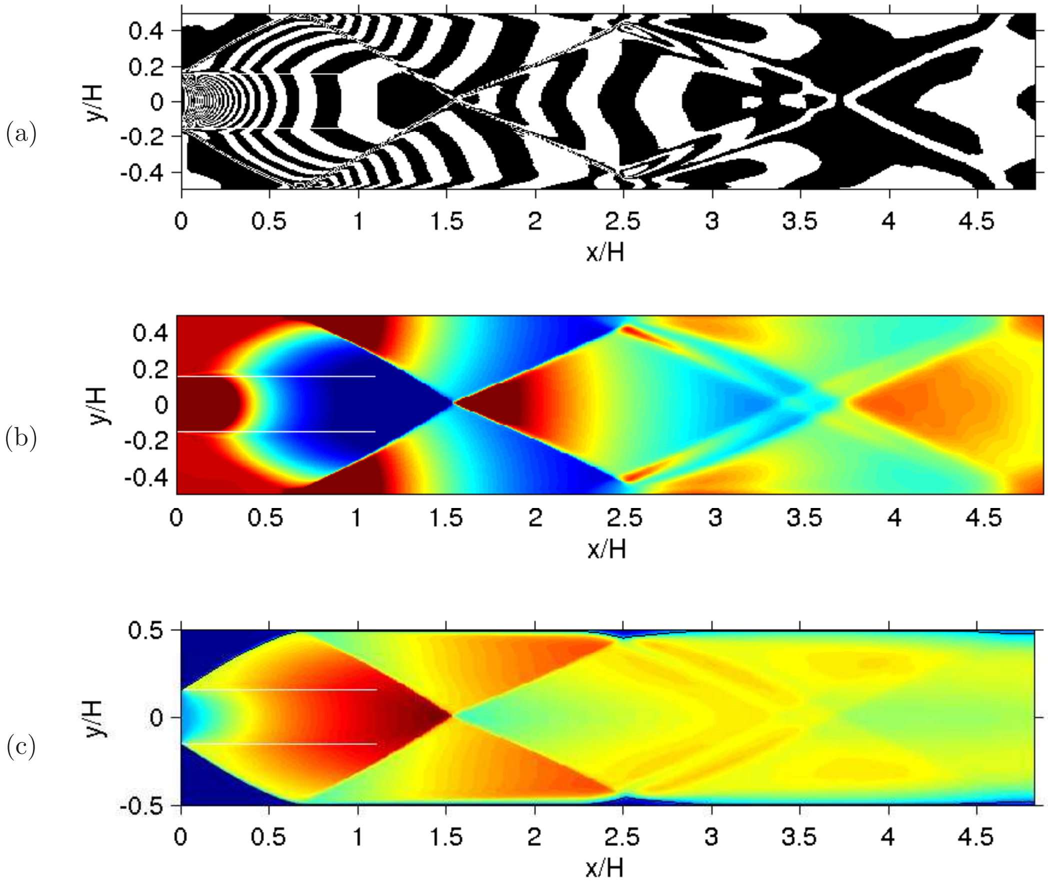

Figure 4. Computed mean flow properties for pressure ratio $\tau = 0.15$: (a) iso-contours of mean density $\bar{\rho}$ using a Mach-Zehnder Interferometrie like colormap; (b) mean pressure field (scale from 2000 Pa to 10000 Pa); (c) mean Mach number field (scale from 0 to 3.7).

Reynolds number based on the nozzle height h and the inflow velocity u_{in} is $\text{Re}_h = 2.1 \times 10^5$. Along the walls of the expansion duct, adiabatic no-slip boundary conditions are imposed.

The pressure in the downstream reservoir $p_e = 17225$ Pa is fixed by the pressure ratio $\tau = 0.15$. The temperature in the downstream reservoir is given by $T_e = T_a = 293$ K. The non-reflective boundary conditions of Tam and Dong,[17] extended to 3-D by Bogey and Bailly,[18] are used along the reservoir boundaries. The turbulent flow leaves the computational domain without spurious acoustic reflections thanks to a sponge zone.[18] Periodic boundary conditions are used in spanwise direction.

The number of 5×10^4 iterations have to be run in order to obtain a converged mean flow field.

2. Results

A plot of mean density iso-contours is represented in Figure 4 (a). Qualitatively the results correspond well to the experiments presented in Figure 2 (a). A divergent supersonic jet formed by the expansion waves generated at the nozzle edges is observed. The first oblique shock wave appears when the expansion waves are reflected by the upper and lower wall. In the computation, the density maximum observed downstream of the jet reattachement is less extended. Further downstream the shock waves are reflected on the lower and upper wall respectively and form a symmetrical cell structure. Figure 4 (b) represents the mean pressure of the flow. The pressure in the corner regions does not match the pressure of the expanding supersonic jet. The mismatch is compensated by a normal shock near the nozzle edges. This can also be observed experimentally. The mean Mach number field, displayed in Figure 4 (c), confirms that the jet core is entirely supersonic and reaches its maximum speed upstream the first shock crossing location. The boundary layer

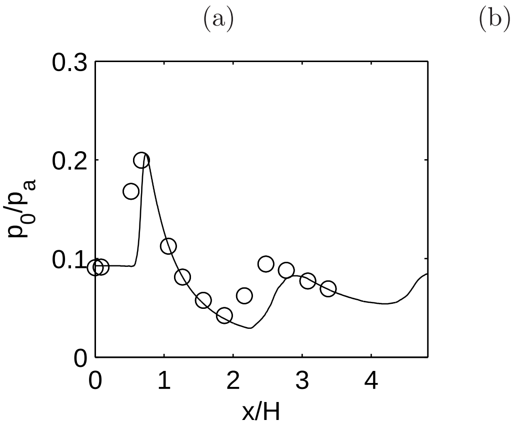

Figure 5. Static pressure distribution along the duct wall, obtained by: ——— the present computation; ○ experiments.[2]

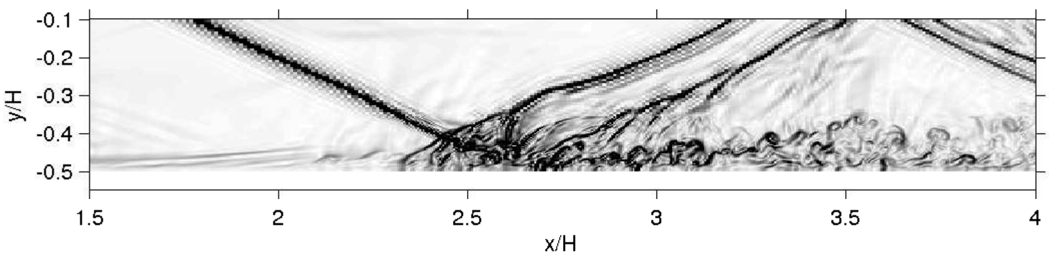

Figure 6. Instantaneous numerical Schlieren field $\nabla\rho$ at the first shock wave/ boundary layer interaction zone.

thickens significantly at the shock reflection points. The flow in the corner region between the jet boundaries and the duct walls remains subsonic.

The computed and measured static mean pressure $\bar{p}$, normalized by p_a, along the lower wall are displayed in Figure 5. The computed and experimental curve compare well qualitatively. The first pressure peak caused by the jet reattachement is accurately predicted even though the peak is too narrow. The subsequent expansion fits very well with the experimental curve. A second compression indicating the reflection of the oblique shock is also well predicted in its amplitude but is located too far downstream and deviates about 10% from the experimental location. This deviation is attributed to a difference of 2% of the computed and experimental pressure in the corner regions. This pressure indeed determines the entire flow regime in the downstream part of the expansion duct. In general higher corner pressures lead to smaller expansion angles and more inclined shock waves are generated when the jet reattaches.

A boundary layer develops along the duct walls where the jet reattaches and interacts with the impinging oblique shock waves. Complex phenomena occur in such configurations as described in the review article of Dolling.[19] A visualization of the instantaneous numerical Schlieren field is given in Figure 6. The incoming boundary layer seems to be transitional. Shock wave/ boundary layer interactions are observed and the downstream boundary layer is more turbulent. This mixing enhancement is typical for such interactions.[20]

A detailed view on the first shock-wave boundary layer interaction on the lower wall is given in Figure 7 (a) representing the iso contours of the time averaged pressure $\bar{p}$. Consistent with experimental observations the incident shock is deviated towards the wall when entering the boundary layer and the reflected shock originates well upstream of the nominal impingement point due to the viscous interaction mechanism. A thickening of the boundary layer and small separation bubble can be observed. The iso-contour lines of specific turbulent kinetic energy $k = (\overline{u'^2} + \overline{v'^2} + \overline{w'^2})/2$ and of $\tau_{xy}/\rho = \overline{|u'v'|}$, the turbulent shear stress, are represented in Figure 7 (c) and (d) respectively. The plot shows that the turbulent kinetic energy k takes its maximum near the point of separation as observed by Pirozzoli *et al.*[21] The turbulent shear stress reaches

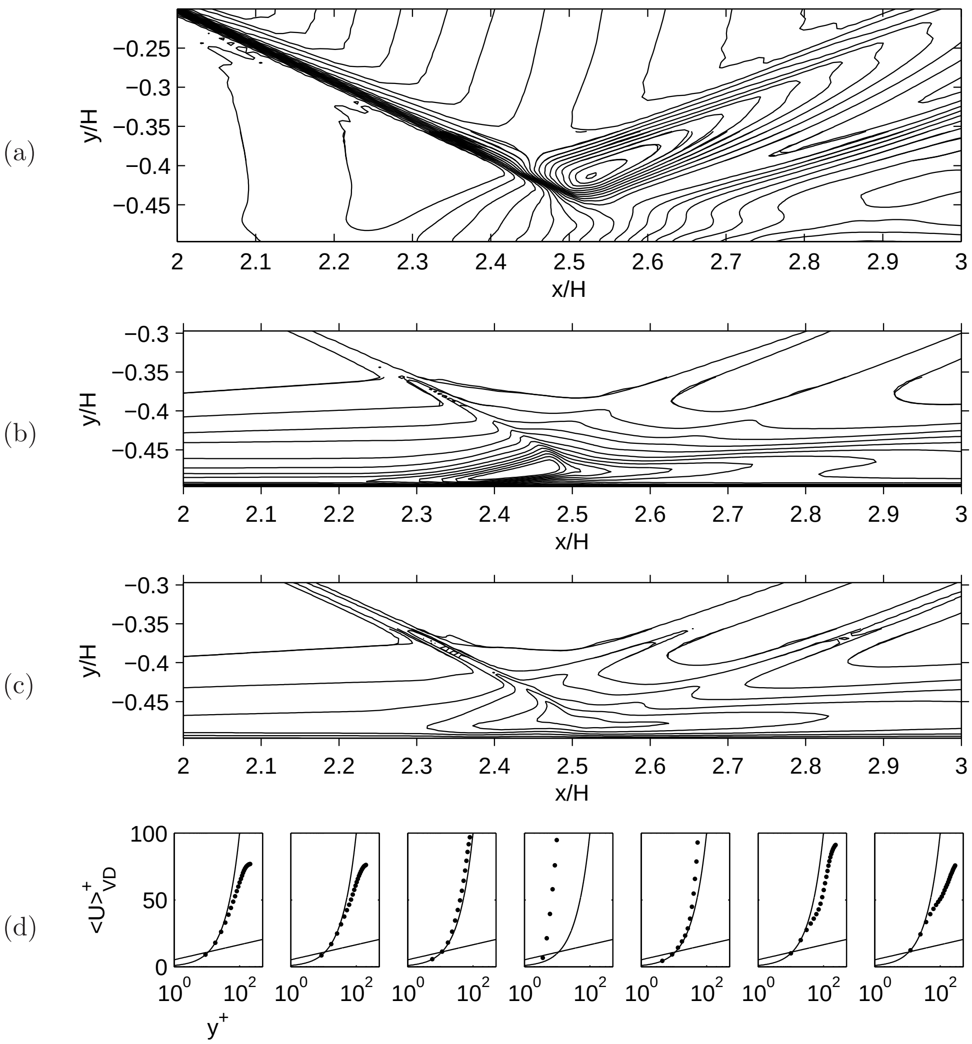

Figure 7. Detail view of the first shock wave/ boundary layer interaction: (a) computed mean pressure contours (31 contours spaced between 2000 and 10000 Pa); (b) iso contours of the turbulent kinetic energy k ranging from ; (c) iso contours of the shear stress τ_{xy}/ρ ranging from ; (d) 7 van Driest transformed velocity profiles at 7 position uniformly distributed between $2 \leq x/H \leq 3$.

its maximum in the vicinity of the shock foot of the incident shock wave.

The van Driest transformed velocity profiles are plotted at seven stations along the lower wall and are provided in Figure 7 (d) using a semilogarithmic scaling. Classically for equilibrium, zero-pressure-gradient, turbulent boundary layers, the mean velocity profile has a linear behavior $u^+_{\mathrm{VD}} = y^+$ for $y^+ \leq 5$ and a logarithmic behavior in the overlap layer $u^+_{\mathrm{VD}} = 0.42 \log{(y^+)} + 5.2$ for $10 \leq y^+ \leq 30$. The linear behavior is well captured by the computation. However the logarithmic behavior is not found in the computation. Grid convergence studies are currently in work, in order to check if this could be due to a not sufficient grid resolution.

Beside these discrepancies, the present code is able to capture viscous as well as inviscid features of the flow. The passage of the oblique shock through the interpolation zone along $y/H \approx 0.3$ happens without creating spurious oscillations as they normally emerge when Lagrangian polynomials of higher-order come into play. The selective filter and the non-linear filter seems to eliminate those spurious modes efficiently. In the following the expansion of a transonic flow for higher pressure ratios is presented.

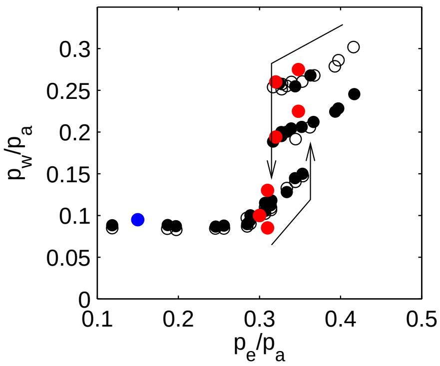

Figure 8. Static mean pressure measured in the corner region (○ upper wall • lower wall) as a function of the pressure ratio τ: in black experimental values;[2] in red and blue the computed values for a duct of length $L = 0.16$ m and $L = 0.24$ m respectively.

IV. Transonic flow at high pressure ratios ($0.30 \leq \tau \leq 0.348$)

3. Experimental observations

The influence of the pressure ratio on the mean flow field has been investigated by Meier *et al.* for various duct geometries. Due to computational limitations, the following numerical study is done using the same duct as in the previous section, but with a reduced length $L = 0.16$ m. Figure 8 shows the normalized time averaged pressure $\bar{p}_w$ at the bottom and top corner region as a function of the pressure ratio τ, where $\bar{p}_w$ denotes the base pressure.

The mean base pressure $\bar{p}_w$ remains constant for low pressure ratios $\tau \leq 0.25$. Their values on both sides of the duct are the same and the flow is therefore symmetrical. The supersonic flow presented in section III is an example of this flow pattern. The computed base pressure is marked with a blue dot obtained for the longer duct. Above $\tau = 0.25$ the corner pressure increases on both sides. For this pressure ratio range, the oblique shock system has completely broken down. In the range from $0.305 \leq \tau \leq 0.352$ a large amplitude oscillation in the corner region can occur. Those large oscillations are associated with the coupling of the shock motion with the longitudinal duct modes such as described in the introduction. When these oscillations exist, the base pressure on both sides are low and of the same order of magnitude. The symmetrical flow is shown in Figure 2 (b).

With pressure ratios $0.316 \leq \tau \leq 0.352$ an additional flow pattern may occur in which the flow is asymmetrical and attached either to the top or bottom wall of the duct. In contrast to the symmetrical case, for the asymmetrical flow pattern no base pressure oscillations occur for the duct length $L = 0.16$ m. Figure 8 shows that two different base pressure values exist for the asymmetrical flow pattern: a lower value for the attached side and a higher value for the unattached side. No preferred attachment location to either the top and the bottom side has been observed experimentally.

The existence of the symmetrical, oscillating flow pattern or the asymmetrical, steady flow pattern depends whether the flow is driven with an increasing or a decreasing downstream pressure. In the experiments the symmetrical oscillating flow pattern exist for an increasing pressure ratio until $\tau = 0.352$ and switches to an asymmetrical flow pattern. When the pressure ratio decreases the asymmetrical flow pattern switches to the oscillating flow pattern at $\tau = 0.316$. This hysteresis is indicated in Figure 8 by the arrows.

Four simulations with pressure ratios $\tau = 0.30$, $\tau = 0.31$, $\tau = 0.32$ and $\tau = 0.348$ have been carried out in order to check if it is possible to capture the symmetric flow pattern. As observed experimentally for this duct geometry aeroacoustic coupling between shock motion and longitudinal duct modes occurs only with a symmetrical flow.

(a) 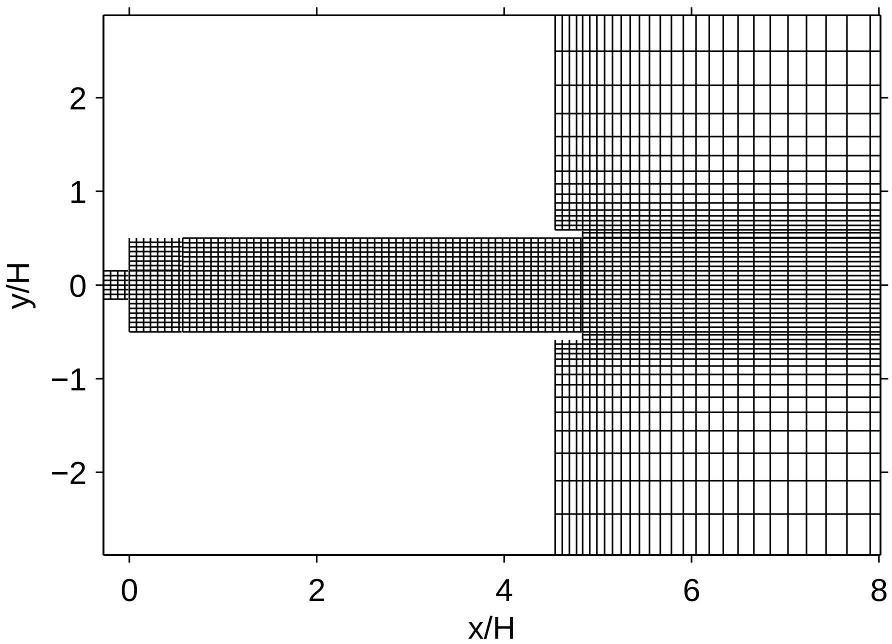

Figure 9. Visualization of the grid in the $x - y$ plane used for the cases of higher pressure ratios $0.30 \leq \tau \leq 0.348$. The geometric parameters are L $= 0.16$ m, L/H $= 5.23$ and h/H $= 0.3$. Every eighth grid line is represented.

4. Simulation parameters

The grid is presented in Figure 9 modelling a duct of length $L = 0.16$ m. Due to numerical limitations, no grid refinement near the duct walls are used for this study. The grid spacings are the same as in section III and are summarized in Table 2. The boundary conditions are applied as in the previous section. The same sonic inflow conditions as in section III are used. The pressure ratios $\tau = 0.30$, $\tau = 0.31$, $\tau = 0.32$ and $\tau = 0.348$ impose exit pressures of $p_e = 30398$ Pa, $p_e = 31411$ Pa, $p_e = 32424$ Pa and $p_e = 35261$ Pa respectively. The temperature in the exit reservoir is given by $T_e = T_a = 293$ K.

	N_x	N_y	N_z	Δx^+_{min}	Δy^+_{min}	Δz^+_{min}	N_{procs}
Nozzle	29	49	21	24	16	24	1
Expansion duct	490	161	21	24	16	24	15
Reservoir	180	398	21	24	16	24	16

Table 2. Grid parameters for the high pressure ratio cases $0.30 \leq \tau \leq 0.348$. All these cases have been computed using $N_{\mathbf{procs}} = 32$ processors. The total number of grid points is 5.0×10^6.

5. Influence of the pressure ratio on the mean flow field

The results of the four different computations are gathered in this section:

- $\tau = 0.30$:

  A rendered 3-D visualization of iso-surfaces of instantaneous numerical Schlieren and vorticity (spanwise component ω_z) is given in Figure 10 (a). The flow features a strong normal shock wave. The flow is symmetrical and the normal shock interacts with the attaching jet by forming a bifurcating or lambda shock on the lower and upper wall. The front leg of the bifurcation is the oblique shock wave that is generated when supersonic jet is deflected by the duct walls. The upstream leg must exist to give proper continuity of the flow direction. Supersonic layers start at the lambda shock and are attached to the upper and lower duct wall. In the vortex sheet, separating the supersonic near wall layers and the subsonic flow in the duct center, 2-D instability rolls develop. These instabilities give rise to turbulent 3-D structures near the duct outflow. The plot of mean Mach number in the $x-y$ plane in Figure 12 (a) confirms that the flow downstream the normal shock is subsonic. The flow downstream the lambda shock keeps being supersonic up to $x/H \approx 3$. The averaged shock position is smeared, due to large shock motions. Figure 11 (a) shows the iso contours of the time averaged density, using a Mach-Zehnder Interferometrie like colormap. The normalized static mean pressure computed along the lower and upper wall is plotted in Figure 15. The wall pressure curves show a symmetrical behavior. The pressure is constant in the base region and increases in the reattachement zone. The pressure exhibits its maximum further downstream at $x/H \approx 2$ and matches the downstream reservoir pressure at the end of the duct. The pressure in the base region at $x = 0$ is plotted in Figure 8 and is in very good agreement with the experimental values.

- $\tau = 0.31$:

  An increase of the reservoir pressure p_e leads to an asymmetrical flow as Figure 10 (b) illustrates. A slightly inclined normal shock can be observed. At the lower wall the normal shocks ends up with a lambda structure situated more upstream than in the $\tau = 0.30$ case. The 2-D vortex rolls develop further downstream. 3-D turbulent structures can already be observed at $x/H \approx 3.4$. On the upper wall the jet is separated from the wall. The jet shear layer is thickened thanks to instability development. The mean Mach number field displayed in Figure 12 (b) shows the inclined normal shock configuration. The upper supersonic layer is separated from the wall, is more extended in downstream direction and thicker than the lower one. The turbulent character of the this flow is illustrated in Figures 13 (a) and (b) showing the turbulent kinetic energy $k = (\overline{u'^2} + \overline{v'^2} + \overline{w'^2})/2$ and the turbulent shear stresses $\tau_{xy}/\rho = |\overline{u'v'}|$ respectively. High levels are localized along the upper jet shear layer. They reach a maximum in the interaction zone with the normal shock. Less turbulent energy is produced on the lower side. The turbulent level grows near the walls and along the vortex sheets and reaches a saturation in the last quarter of the duct. The mean pressure computed along the upper and lower wall are given in Figure 15 (b). The pressure in the lower corner region reaches a value similar to the one obtained for lower pressure ratios. The subsequent compression is caused by the shock that is located slightly more upstream as in the upper case. The pressure in the upper corner region is increased and the compression takes place further downstream. The base pressures are also plotted in Figure 8 and agree well with the experiment. This kind of asymmetry was observed in the experiments only for longer ducts.

- $\tau = 0.32$:

  Figure 10 (c) shows the flow pattern obtained for $\tau = 0.32$. The flow is asymmetric and is separated entirely from the lower duct wall. The iso-surfaces of vorticity shows how the jet cross-section is initially intact and how it begins to break up and mix more efficiently at the middle of the first shock cell. On the lower wall regularly spaced strong perturbations that travel upstream can be observed. The Mach number field given in Figure 12 (c) exhibits two shock cells and a reversed flow is found on the lower duct wall. The jet reattaches after the end of the second shock cell. No major jet spreading can be observed such as observed for free jets. Turbulence data given in Figure 14 (a) and (b) show high turbulent kinetic energy production along the upper and lower shear layers. On the attached side turbulent production is endorsed by the presence of the wall. On the lower wall the turbulent energy has reached its maximum downstream the first shock and drops to a constant stagnant value up to the end of the duct. This indicates a transition to a fully turbulent flow. The static mean pressure along the upper and lower wall are plotted in Figure 15 (c). The pressure at the duct end on the upper wall matches the reservoir pressure after the sequence of expansion and compression waves . The pressure curve at the lower duct wall does not feel the presence of the shock and increases slowly and ends up to match the reservoir pressure. Figure 8 reveals the excellent agreement of the normalized base pressures with the upper branch of the experimentally measured curve.

- $\tau = 0.348$:

  The flow pattern of this pressure ratio is very similar to the case with $\tau = 0.32$. The jet is attached on the upper wall. The jet expansion angle is smaller due to the increased pressure ratio. As shown in Figure 8, the pressure computed in the corner region are slightly over estimated compared to experiments.

6. Unsteady flow aspects

The pressure signals recorded along the upper wall are examined for the flows computed for the pressure ratios $\tau = 0.31$ and $\tau = 0.32$. Signals recorded at the corner and at the duct end are plotted in Figure 16. For $\tau = 0.31$ regular small amplitude oscillations in the base region are observed. At the duct end, turbulent broadband noise dominates. Sound pressure levels are provided in Figure 17 (a) at the positions $x = 0$, $x = L/2$ and $x = L$. Low frequency components, at $x = 0$ and at $x = L/2$, are observed. Those components are not present at the end of the duct. The pressure spectra reveal a high frequency component at $f \approx 5000$ Hz. This frequency is associated to the transverse duct modes that are excited by the turbulent broadband noise. For $\tau = 0.32$ no low frequency oscillations can be observed. A frequency $f \approx 1500$ Hz is dominant. The high-frequency mode at $f \approx 5000$ Hz is also observed for this pressure ratios.

No areoacoustic coupling is detected by the present simulation. This is consistent with the experiments that does not exhibit aeroacoustic coupling when the asymmetric transonic flow regime is established in the duct. The dominance of the asymmetric flow pattern seems to be caused by the application of periodic boundary conditions in the spanwise direction. The pressure in the upper and lower corner regions cannot be kept in balance as it would be the case when the lateral walls are present: the jet destabilizes and attaches to one duct side more easily.

V. Conclusion

A numerical algorithm is proposed to deal with transonic and supersonic flows. An optimized finite difference scheme with low numerical dispersion and dissipation is combined with a selective high-order filtering. An additional non-linear low-order filter applied to the shock region. First, the expansion of a transonic flow in a rectangular duct is computed for a pressure ratio leading to an entirely supersonic flow. The aerodynamic field is found to be in good agreement with experiments. Second, several simulations of the same configuration for different pressure ratios, where coupling between normal shock motion and longitudinal duct modes are likely to occur, are presented. An investigation of the influence of pressure ratio on the mean flow field shows that the present numerical algorithm is able to reproduce the main flow patterns in a satisfying way. The abrupt switch from symmetrical to asymmetrical flow pattern is well predicted and follows the hysteresis branch obtained for decreasing pressure ratios. The asymmetric flow pattern is the preferred configuration of the numerical simulation. No aeroacoustical coupling is observed for the asymmetrical flow pattern in agreement with experiments,

Acknowledgments

Thanks to William Henshaw (Lawrence Livermore National Laboratory) for providing useful advices about the *Overture* library.

References

[1]Meier G.E.A., Szumowski A.P. and Selerowicz W.C. *Self-excited oscillations in internal transonic flows.* Progress in Aerospace Sciences, **2** (1990), 145-200.

[2]Meier G.E.A., Grabitz G., Jungowski W.M., Witczak K.J and Anderson J.S. *Oscillations of the supersonic flow downstream of an abrupt increase in duct cross-section.* Mitteilung aus dem Max-Planck-Institut fuer Stroemungsforschung und der Aerodynamischen Versuchsanstalt, **65** (1978), 1-172.

[3]Tam C.K.W. *Computational Aeroacoustics: An overview of Challenges and Applications.* International Journal of Computational Fluid Dynamics, **18** (2004), 547 - 567.

[4]Lafon P., Devos J. P. *Numerical prediction of instabilities in transonic internal flows using an Euler TVD code.* AAIA Paper, (1993) 1993-72.

[5]Visbal M.R., Gaitonde D.V. *On the use of higher-order finite-difference schemes on curvilinear and deforming meshes.* Journal of Computational Physics, **181** (2002), 155-185.

[6]Marsden O., Bogey C. and Bailly C. *High-order curvilinear simulations of flows around non-cartesian bodies.* Journal of Computational Acoustics, **13**(4) (2005), 732-748.

[7]Schlichting H. *Boundary Layer Theory.* McGraw-Hill, Inc., (1979), 328.

[8]Bogey C., Bailly C. and Juvé D. *A family of low dispersive and low dissipative schemes for Large Eddy simulations and for sound propagation.* Journal of Computational Physics, **194** (2004), 194-214.

[9]Bogey C., Bailly C. *Large Eddy Simulations of transitional round jets : influence of the Reynolds number on flow development and energy dissipation.* Physics of Fluids, **18** (2006), 1-14.

[10] Gaitonde D.V., Visbal M.R. *Advances in the application of high-order techniques in simulation of multi-disciplinary phenomena.* International Journal of Computational Fluid Dynamics, **17** (2003), 95-106.

[11] Kim J.W., Lee D.J. *Adaptive non-linear artificial dissipation model for Computational Aeroacoustics.* AIAA Journal, **39** (2001), 810-818.

[12] Jameson A., Schmidt W. and Turkel E. *Numerical simulation of the Euler equations by finite volume methods using Runge-Kutta time stepping schemes.* AIAA Paper, (1981) 81-1259.

[13] Benek J.A., Steger J.L. and Dougherty F.C. *A flexible grid embedding technique with applications to the Euler equations.* AIAA Paper, 83-1944 (1983).

[14] Delfs J.W. *An overlapped grid technique for high resolution CAA schemes for complex geometries.* AIAA Paper, 2001-2199.

[15] Henshaw W. D. *Ogen: an overlapping grid generator for Overture.* http://www.llnl.gov/casc/Overture.

[16] Sherer S.E., Scott J.N. *High-order compact finite-difference methods on general overset grids.* Journal of Computational Physics, **210** (2005), 459 - 496.

[17] Tam C.K.W., Dong Z. *Radiation and outflow boundary conditions for direct computation of acoustic and flow disturbances in a nonuniform mean flow.* Journal of Computational Acoustics, **4** (1996),175-201.

[18] Bogey C., Bailly C. *Three-dimensional non-reflective boundary conditions for acoustic simulation: far field formulation and validation test cases.* Acta Acustica United With Acustica, **88** (2002), 463-471.

[19] Dolling D.S. *Fifty years of shock-wave/ boundary layer interaction research: what next ?* AIAA Journal, **39** (2001), 1517.

[20] Smits A.J. Dussauge J.P. *Turbulent Shear Layers in Supersonic Flows, second edition.* Springer, NY, (2006).

[21] Pirozzoli S., and Grasso F. *Direct numerical simulation of impinging shock wave/turbulent boundary layer interaction at M=2.25.* Physics of Fluids, **18** (2006) 065113.

[22] Lafon P., Caillaud S., Devos J.P. and Lambert C. *Aeroacoustical coupling in a ducted shallow cavity and fluid-structure effects on a steam line.* Journal of Fluids and Structures, **18** (2003) 695-713.

[23] Rockwell D. *Oscillations of impinging shear layers.* AIAA Journal, **21** (1983) 645-664.

[24] Shieh C. M., Morris P. J. *Parallel computational aeroacoustic simulation of turbulent subsonic cavity flow.* AIAA Paper, (2000) 2000-1914.

[25] Bogey C. Gloerfelt X. and Bailly C. *Numerical evidence of mode switching in the flow-induced oscillations by a cavity.* Int. J. of Aeroacoustics, **2**(2) (2003), 99-124.

[26] Lafon P., Devos J. P. *Computation of the noise generated by a shallow cavity and test of a solution for lowering the noise.* AAIA Paper, (2003) 2003-3105.

[27] Amandolese X., Hemon P., and Regardin C. *Study of the acoustic oscillations by flows over cavities. Part1. Internals flows.* Proceedings of the Fifth International Symposium on Fluid-Structure Interactions, IMECE'02, New Orleans, (2002).

[28] Rossiter C.W. *Wind-tunnel experiments in the flow over rectangular cavities at subsonic and transsonic speeds.* Aeronautical Research Council Reports and Memoranda, Technical Report 3438.

A. Ducted cavity flow

A. Introduction

This configuration has been first studied for an industrial application.[22] A pure tone acoustic phenomenon has been observed on the power steam line of a nuclear power station and a cavity located in a gate valve has been identified as the noise source. This cavity has two specific characteristics: it is confined and partially covered.

It is well known that a flow past a cavity gives rise to noise radiation. A complex feedback process between the upstream and downstream corners produces coherent oscillations in the shear layer developing above the cavity.[23–25] For cavities in open space, the oscillations remain weak at low Mach numbers. Therefore most published papers are adressed to cavity subsonic flows in the upper Mach number range. For ducted cavities, the possible coupling between cavity oscillations modes and duct acoustic modes can lead to high amplitude oscillations even at low speeds. This coupling mechanism is associated to the lock-in phenomenon.

Due to the geometry of the valve, a simplified 2-D model was studied experimentally and numerically.[22,26] The retained geometry is reported in Figure 18. Lafon *et al.*[26] used a second-order TVD scheme for solving 2-D Euler's equations. Peak frequencies were well captured but not the flow details due to 2-D artefacts of the simulation.

In the present work 3-D compressible Navier-Stokes equations are solved using the algorithm described in section II. It is expected that more flow details should be retrieved. The experimental results obtained in the previous studies of ducted cavities[22,27] are used to validate the numerical tool. In particular the coupling between cavity modes and transverse duct modes is considered.

B. Experimental observations

Details about the experiments are available in previous papers.[22,27] Only the main outlines are recalled here. The characteristic dimensions of the experimental model are : $d = 0.05$ m, $h = 0.02$ m, $H = 0.137$ m, $L = 0.073$ m. The span of the test section has a value of 0.16 m.

Pressure signals have been measured using a microphone located at the bottom center of the cavity. The measured spectra exhibit peaks that can be associated to cavity modes. Plots of frequency and pressure level of these peaks as functions of the nominal Mach number $M_0 = U_0/c_0$ are shown in Figure 19. Figure 20 displays corresponding plots of experimental Strouhal compared to theoretical ones. The modes of the cavity can be estimated by Rossiter's formula:[28]

$$St_R = \frac{fd}{U_0} = \frac{n_R - \xi}{M_0 + U_0/U_c},$$

where $\xi = 0.25$, $U_0/U_c = 0.57$, n_R is the mode number. These modes are associated to the Rossiter's modes (RM) and the second and third modes are plotted in Figure 20. The transverse modes of the duct are given by

$$St_d = f_d \frac{d}{U_0} = \frac{c}{2n_d H} \frac{d}{U_0},$$

where n_d is the duct mode number. The first transverse duct mode (DM) is also plotted in Figure 20.

The frequency of the oscillation locks in the frequency of the pipe mode when Rossiter's mode approaches the duct mode. When lock-in occurs, the pressure level is maximum. At $M = 0.13$, the cavity mode 3 couples with the first transverse duct mode and and at $M = 0.18$, the cavity mode 2 couples with the first transverse duct mode. At $M = 0.23$, the cavity mode 3 locks with the second transverse duct mode. In this case the measured frequencies collapse with the transverse duct mode based on the sum of the duct and cavity height.

C. Simulation parameters

The entire overset grid generated by *ogen* is displayed in Figure 21. It consists of seven component grid. As the grid points of the communication interfaces coincide, no interpolation has to be used. The grid spacing is kept constant in the cavity ($\Delta x = 0.4$ mm and $\Delta y = 0.2$ mm) and in the boundary layer ($\Delta y = 0.2$ mm). In the duct, the grid is stretched in the y-direction near the upper wall with 3.0%. Upstream and downstream of the cavity the grid is stretched in the x-direction with 1.0%.

	N_x	N_y	N_z	N_{procs}
Duct	542	149	41	39
Neck	126	39	41	3
Cavity	180	61	41	5

Table 3. Grid parameters for the ducted cavity. A total number of 4×10^6 grid points has been distributed over $N_{\text{procs}} = 47$ processors.

The crucial point in cavity simulations is the boundary layer upstream the cavity whose shape controls the vortex shedding and the convection of the eddies in the shear layer. The experimental boundary layer profile is fitted by a $1/n$ profile such as:

$$\frac{u_b(y)}{U_0} = \left(\frac{y}{\delta}\right)^{\frac{1}{n}},$$

where $\delta = 8.8$ mm and $n = 8.5$. This profile is imposed as the initial condition. During the simulation the profile is weakly recalled along the inlet boundary condition through the expression:

$$\tilde{u}^{n+1} = u^{n+1} - \sigma_{rc}(u^{n+1} - u_b(y)),$$

where $\sigma_{rc} = 0.005$ has to be kept small to prevent numerical reflections. In order to avoid excessive filtering of the inflow velocity profile, only the fluctuating quantities are filtered. The initial mean flow field upstream the cavity is preserved during the simulation run.

As the flow is in the low subsonic domain, the density and the pressure are taken constant over the whole height of the inflow and outflow ($p_{in} = p_{out} = 10^5$ N/m^2, $\rho_{in} = \rho_{out} = 1.2$ kg/m^3). Like for the velocity profile, the density and the pressure are imposed in a weak manner to anticipate possible numerical drift. An sponge zone combining grid stretching and a Laplacian filter at the outflow are used to avoid reflections.

D. Analysis of the results

Calculations have been carried out for several nominal Mach numbers : $M_0 = 0.13, 0.16, 0.18, 0.20, 0.21, 0.23$ and 0.25. The spectra obtained from signals recorded at the bottom center of the cavity give the frequency and the amplitude of the peaks associated to the second and third cavity modes.

Figure 22 shows the evolution of the computed and measured frequencies of the modes. The frequency of the modes are well retrieved. The lock-in phenomenon can be observed when the frequencies of cavity modes stop their natural evolution and remain "locked" to the duct mode: at $M_0 = 0.13$, lock-in between the 3. RM and 1. DM, at $M_0 = 0.18$, 0.20, lock-in between the 2.RM and 1.DM and at $M_0 = 0.23$, lock-in between the 3. RM and 2. DM occurs. In agreement with the experimental results, in the latter case the coupling occurs rather with the 2. DM mode based on the sum of the duct and cavity height.

Figure 23 compares the computed and measured amplitudes of the cavity modes as a function of the Mach number. The comparison is qualitatively good. However the mode 2. RM remains too high after lock-in having occured at $M_0 = 0.18$, 0.20. The amplitude of 3. RM is too high for low Mach numbers and too low for high Mach numbers. As a consequence, the crossing of the amplitude curves of modes 2. RM and 3. RM at $M_0 = 0.2$ is not reproduced.

Figures 24, 25, 26 show snapshots of the instantaneous pressure field in the duct and vorticity field in the cavity. Figure 25 shows that at $M_0 = 0.20$ (when the mode 2.RM dominates the spectrum), two eddies appear very distinctly in the shear layer. In Figures 24 and 26 this less obvious, because for these two Mach numbers, the 2. and the 3. RM have similar amplitudes.

The present study shows that is possible to reproduce the coupling phenomenon between the cavity modes and the duct modes with the present numerical algorithm. Qualitative discrepancies, in particular the absence of a dominant 3. cavity mode, are currently under examination. Grid convergence studies and the implementation of a fluctuating turbulent inflow boundary condition are planed in the future.

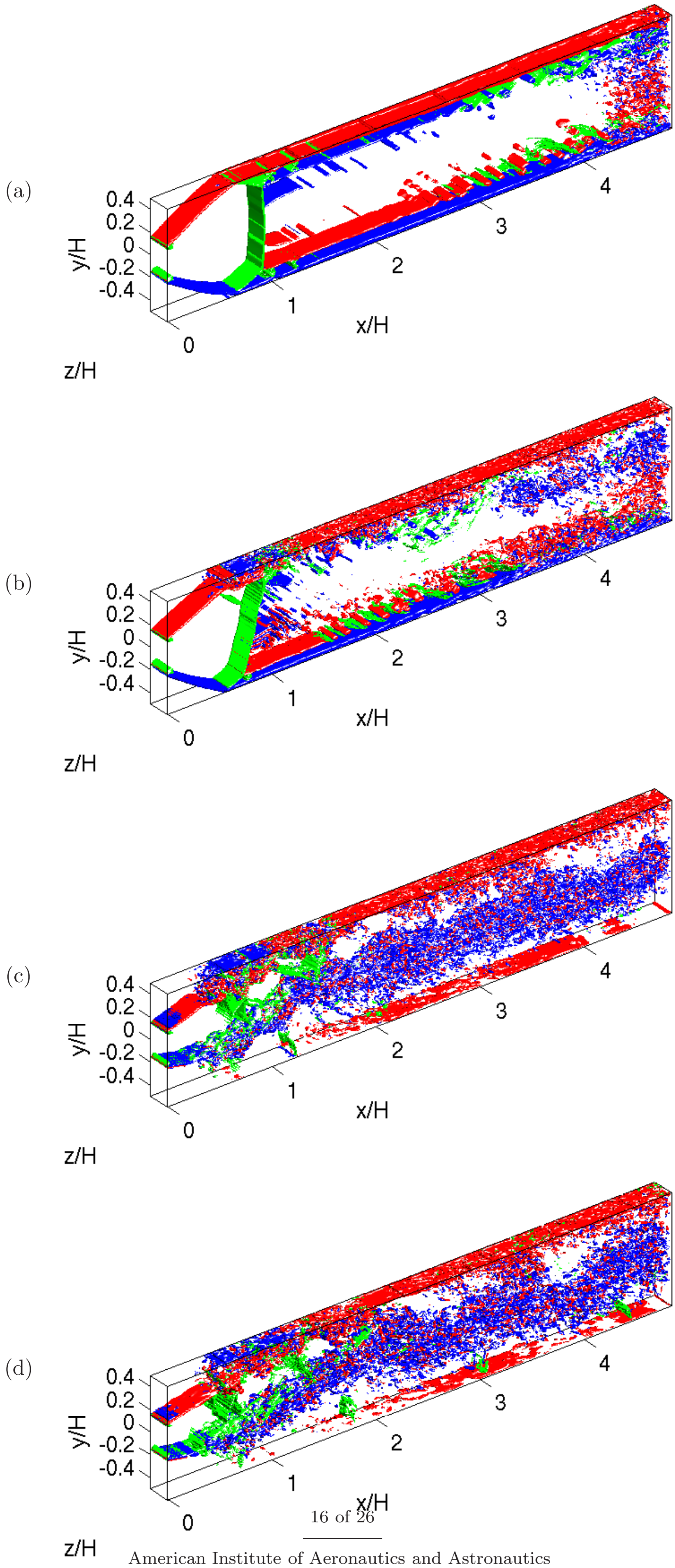

Figure 10. Rendered 3-D view of iso-surfaces: red and blue surfaces represent instantaneous spanwise vorticity field for $\omega_z = +150000$ s^{-1} and $\omega_z = -150000$ s^{-1} respectively, green surfaces represent numerical Schlieren with $\nabla\rho = 200$ kg.m^{-4}.

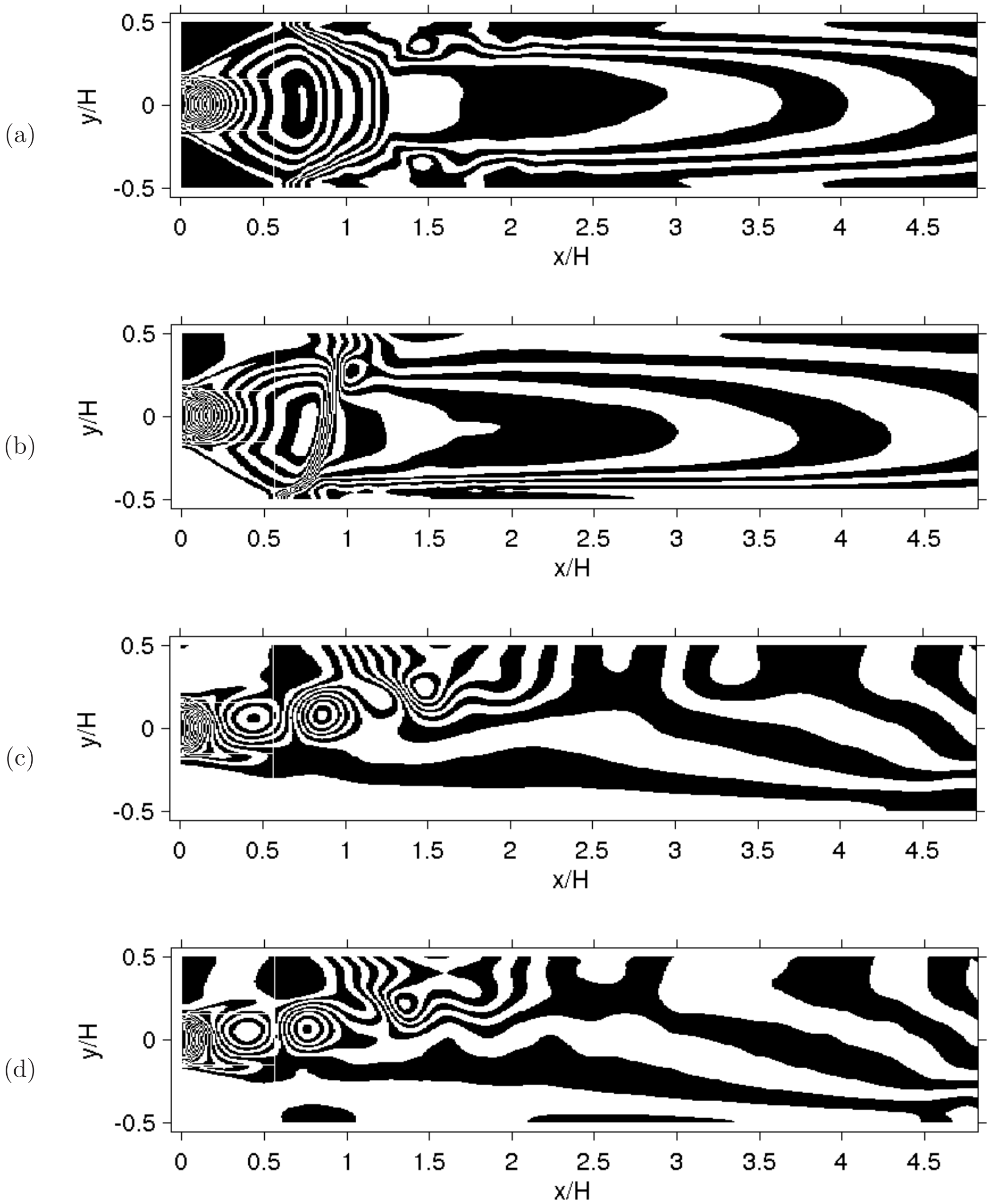

Figure 11. Iso-contours of the mean density $\bar{\rho}$ for different pressure ratios: (a) $\tau = 0.30$, **(b)** $\tau = 0.31$, **(c)** $\tau = 0.32$, **(d)** $\tau = 0.348$.

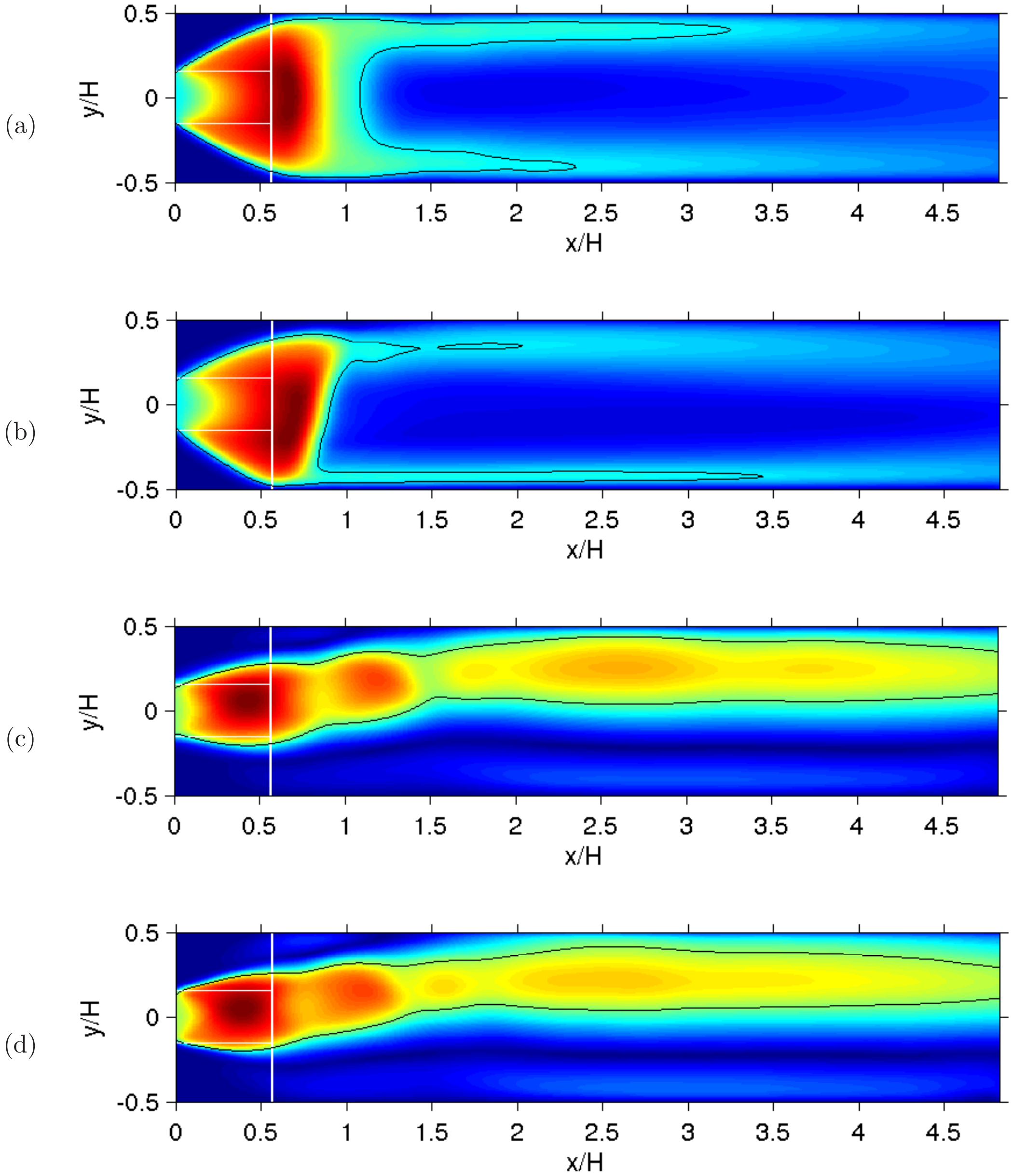

Figure 12. Mean Mach number field $M = |\bar{\mathbf{u}}|/\bar{c}$ for different pressure ratios: (a) $\tau = 0.30$, (b) $\tau = 0.31$, (c) $\tau = 0.32$, (d) $\tau = 0.348$; the color scale lies in the range $0 \leq \bar{M} \leq 2.1$. ——— represents the sonic line $M = 1$.

(a)

(b)

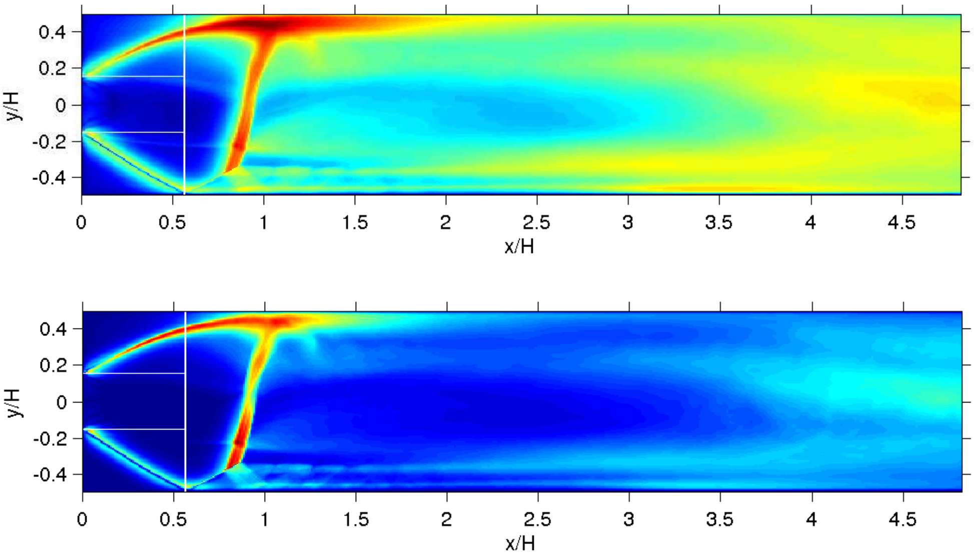

Figure 13. Turbulent data for the pressure ratio $\tau = 0.31$: (a) turbulent kinetic energy: the color scale range from $0 \leq k \leq$; (b) turbulent shear stresses: the color scale range from $0 \leq \tau_{xy}/\rho \leq$.

(a)

(b)

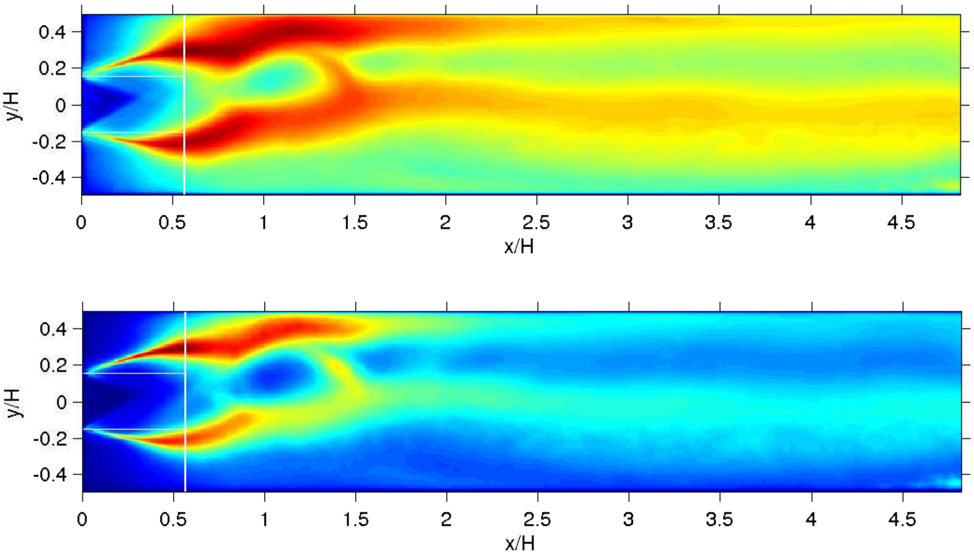

Figure 14. Turbulent data for the pressure ratio $\tau = 0.32$: (a) turbulent kinetic energy: the color scale range from $0 \leq k \leq$; (b) turbulent shear stresses: the color scale range from $0 \leq \tau_{xy}/\rho \leq$.

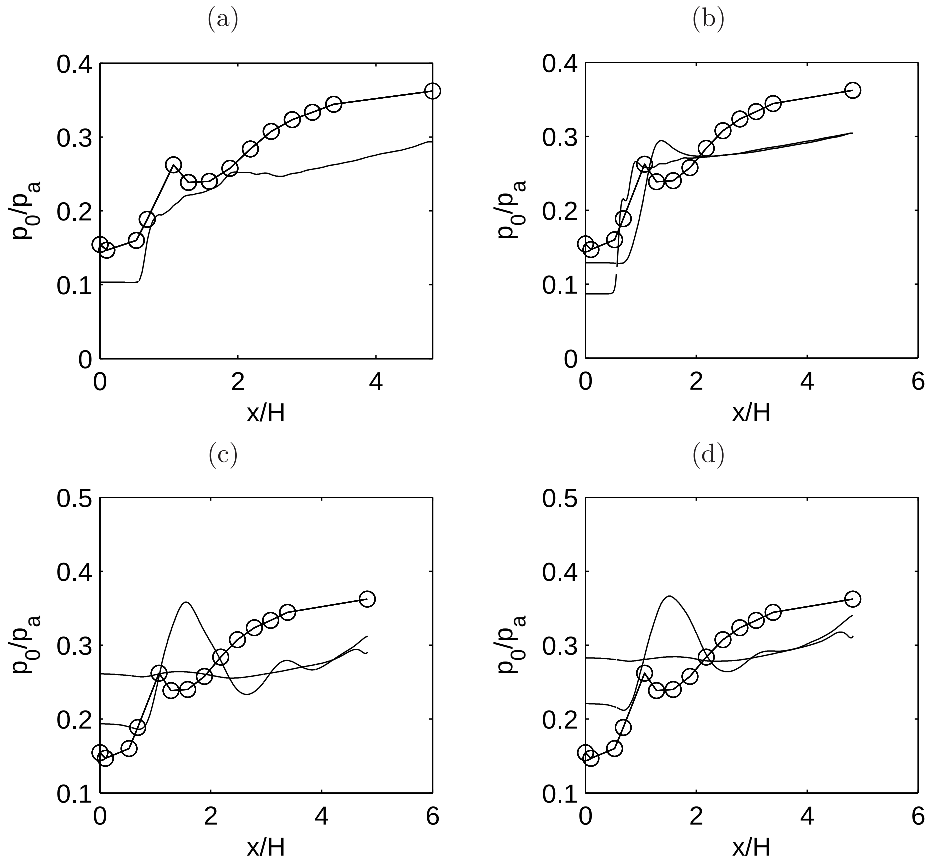

Figure 15. Static mean pressure measured on the lower and upper wall for different pressure ratios: (a) $\tau = 0.30$, **(b)** $\tau = 0.31$, **(c)** $\tau = 0.32$, **(d)** $\tau = 0.348$.

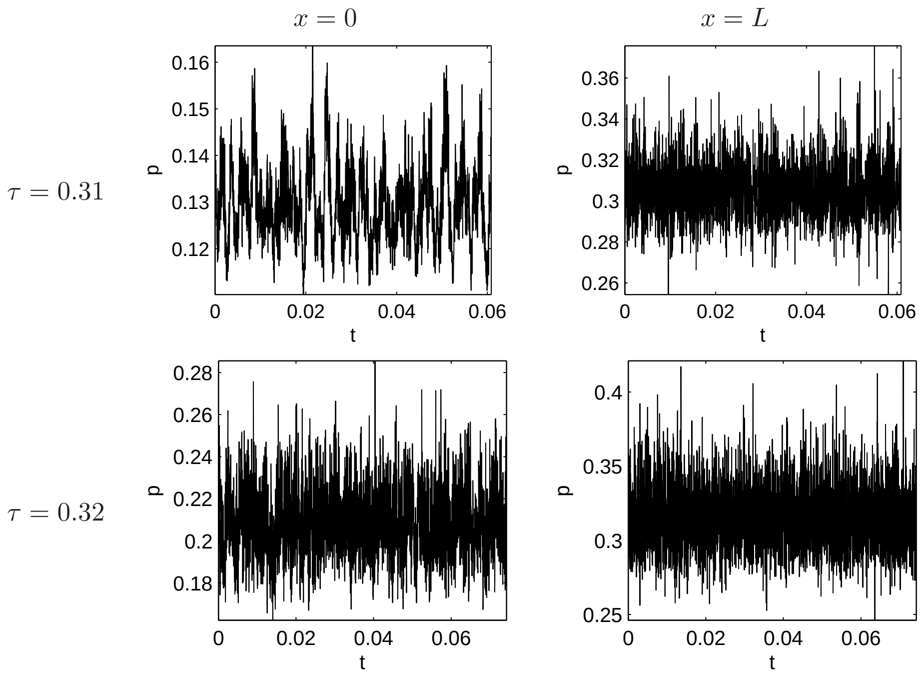

Figure 16. Pressure signals recorded at the upper wall for different pressure ratios: (a) $\tau = 0.30$, (b) $\tau = 0.31$, (c) $\tau = 0.32$, (d) $\tau = 0.348$.

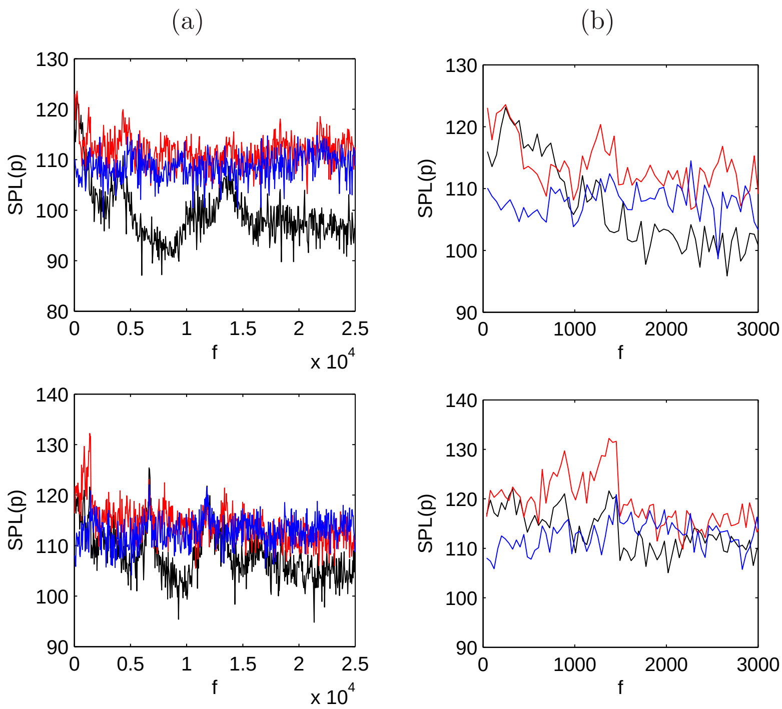

Figure 17. Spectra of pressure signals recorded on the upper wall at three positions ——— $x = 0$, ——— $x = L/2$, ——— $x = L$ **for different pressure ratios (a) $\tau = 0.31$, (b) $\tau = 0.32$.**

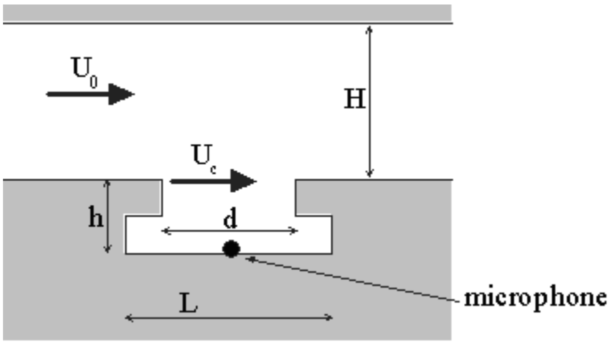

Figure 18. Ducted cavity: sketch of the geometry and notations $d = 0.05$ m, $h = 0.02$ m, $H = 0.137$ m, $L = 0.073$ m. U_0 is the free stream velocity considered as the nominal velocity, U_c is the convection velocity of eddies in the shear layer.

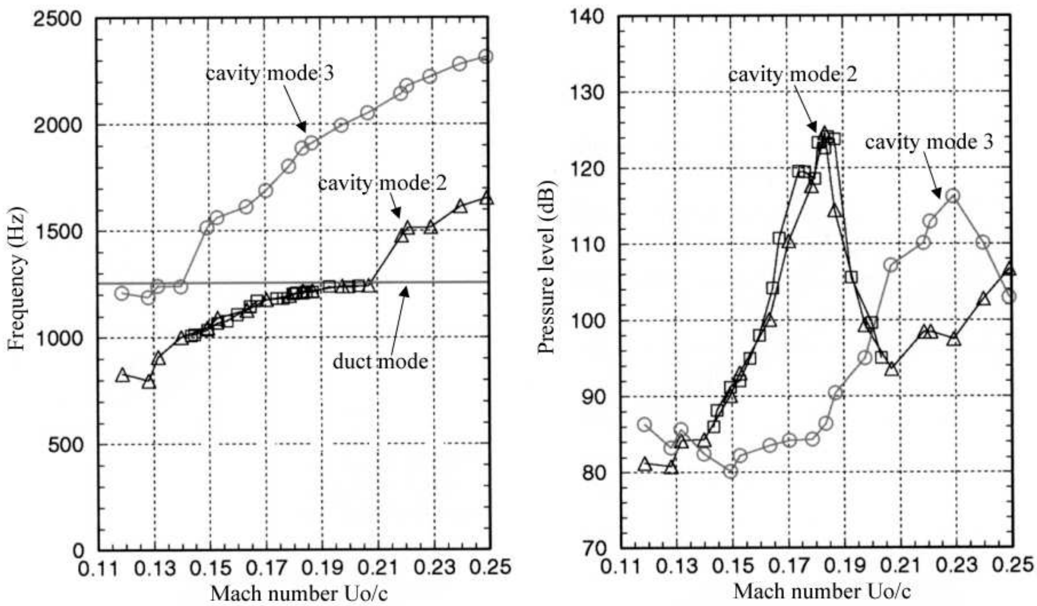

Figure 19. Frequency and pressure level of oscillations measured inside the cavity model as functions of the Mach number.

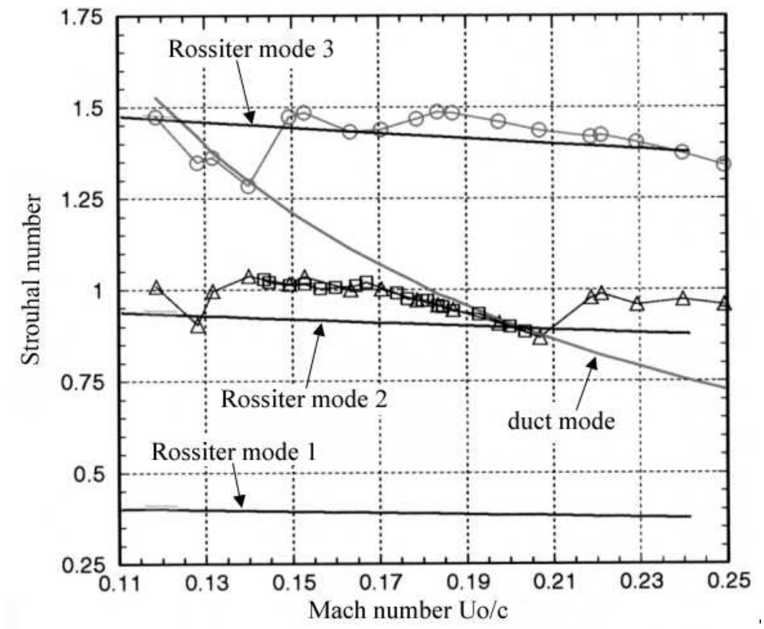

Figure 20. Strouhal number measured inside the cavity model compared to theoretical ones as a function of the Mach number U_0/c_0.

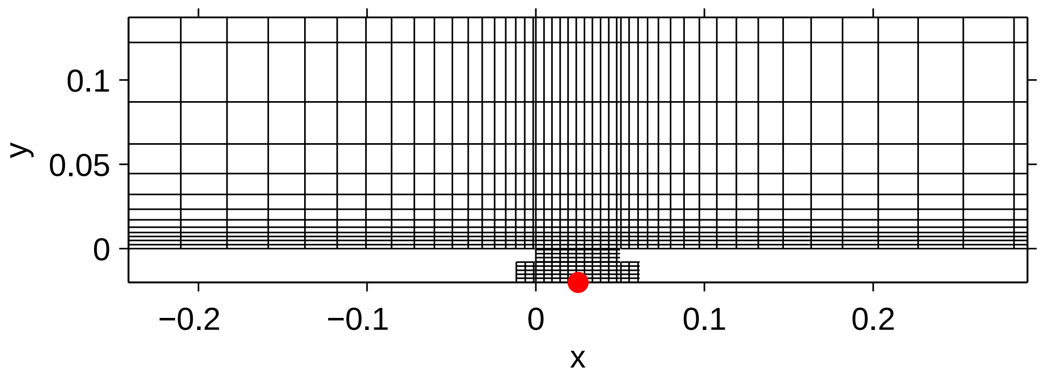

Figure 21. Overset grid generated by *ogen*. Every tenth line is represented.

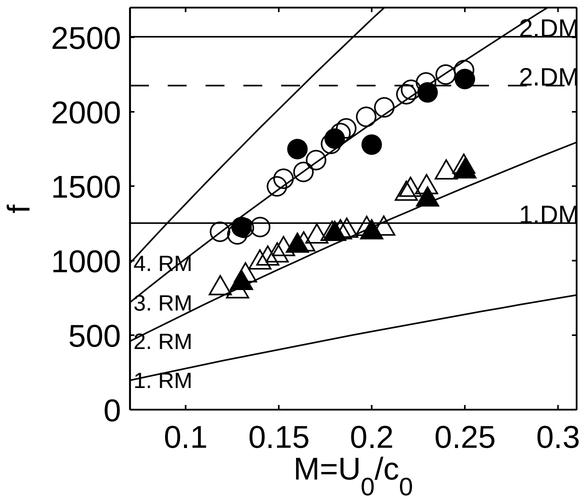

Figure 22. Computed frequencies (mode 2, •, mode 3, ▲) of the cavity modes compared to experimental ones (mode 2, ○, mode 3, △) and to Rossiter's and duct mode frequencies (RM = Rossiter's mode, DM = duct modes). The modified 2.DM (− − −) mode is calculated with the sum of the duct and the cavity heights .

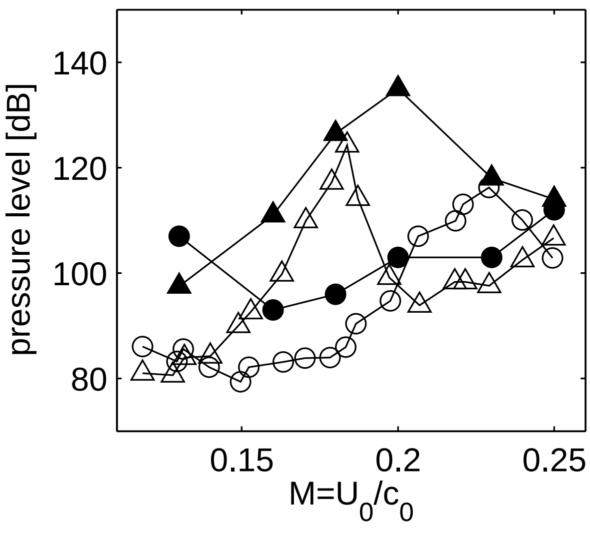

Figure 23. Computed power levels (mode 2, •, mode 3, ▲) of the cavity modes compared to experimental ones (mode 2, ○, mode 3, △).

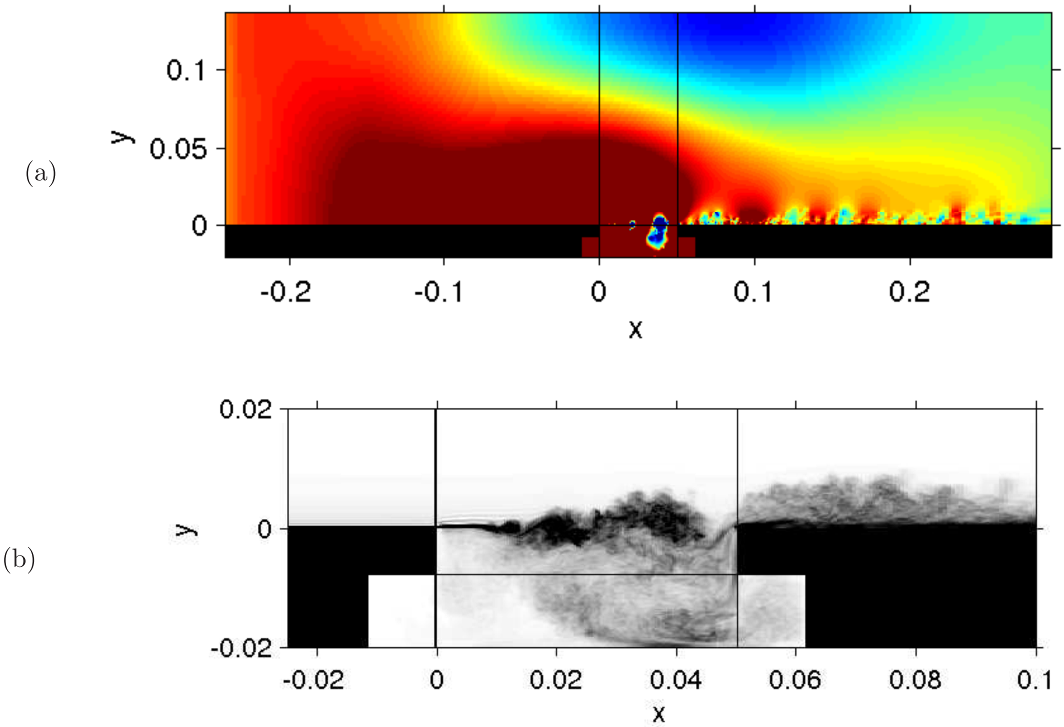

Figure 24. Computed instantaneous results for M=0.13 (a) pressure fluctuations (<100 Pa) in the duct, (b) spanwise averaged vorticity modulus in the cavity

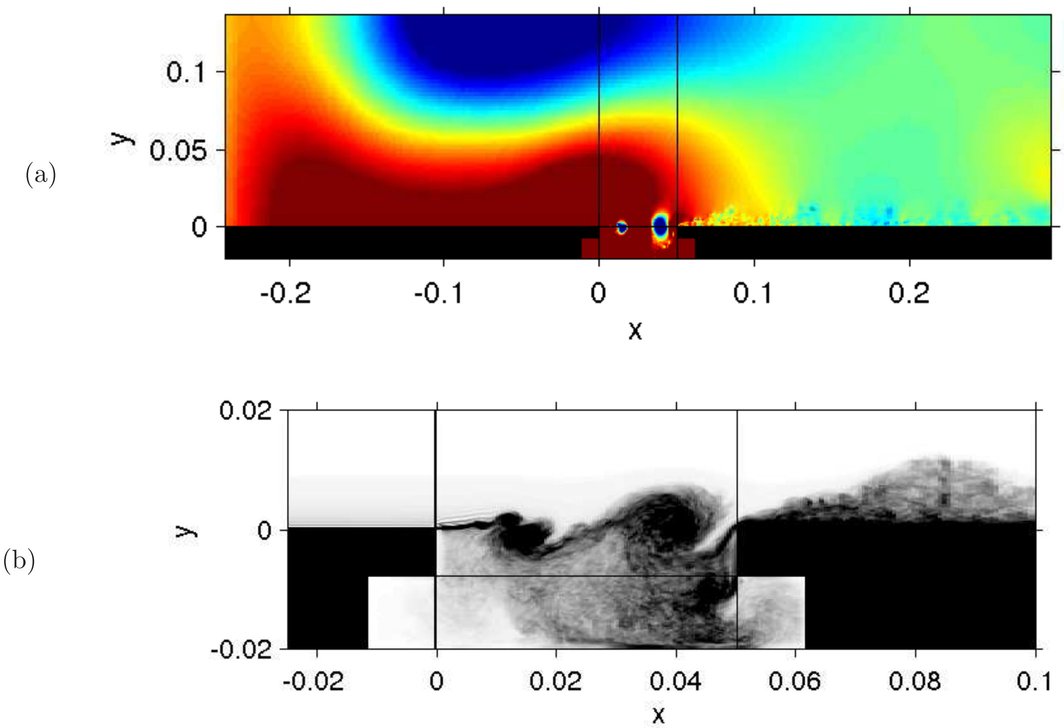

Figure 25. Computed instantaneous results for M=0.20 (a) pressure fluctuations (<100 Pa) in the duct, (b) spanwise averaged vorticity modulus in the cavity

(a)

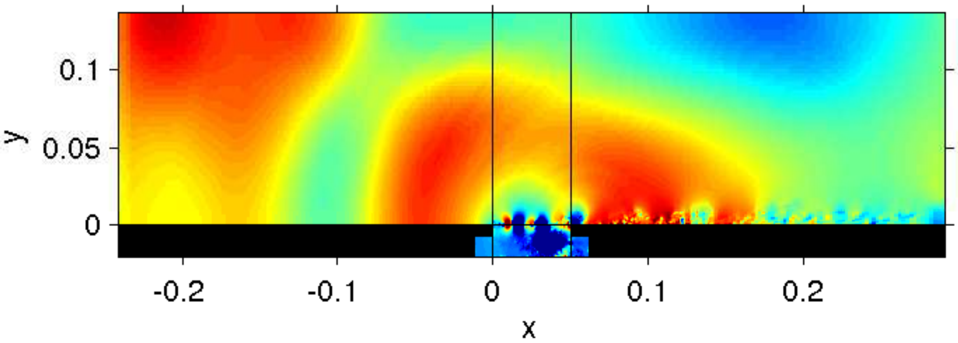

(b)

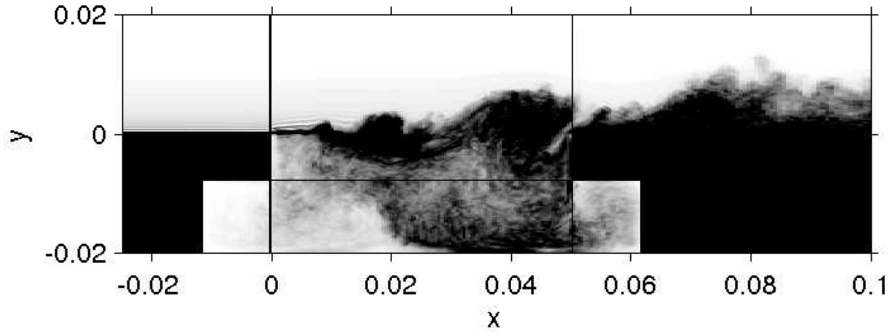

Figure 26. Computed instantaneous results for M=0.25 (a) pressure fluctuations (<100 Pa) in the duct, (b) spanwise averaged vorticity modulus in the cavity